A Dynamic Monte Carlo Model for Predicting Radiant Exposure Distribution in Dental Composites: Model Development and Verifications

Yin-Chu Chen[a], Jack L. Ferracane[b], Scott A. Prahl[a]
[a]Department of Biomedical Engineering, OHSU, Portland, OR
[b]Division of Biomaterials & Biomechanics, OHSU, Portland, OR

ABSTRACT

Photo-cured dental composites are widely used in dental practices to restore teeth due to the esthetic appearance of the composites and the ability to cure in situ. However, their complex optical characteristics make it difficult to understand the light transport within the composites and to predict the depth of cure. Our previous work showed that the absorption and scattering coefficients of the composite changed after the composite was cured. The static Monte Carlo simulation showed that the penetration of radiant exposures differed significantly for cured and uncured optical properties. This means that a dynamic model is required for accurate prediction of radiant exposure in the composites. The purpose of this study was to develop and verify a dynamic Monte Carlo (DMC) model simulating light propagation in dental composites that have dynamic optical properties while photons are absorbed. The composite was divided into many small cubes, each of which had its own scattering and absorption coefficients. As light passed through the composite, the light was scattered and absorbed. The amount of light absorbed in each cube was calculated using Beer's Law and was used to determine the next optical properties in that cube. Finally, the predicted total reflectance and transmittance as well as the optical property during curing were verified numerically and experimentally. Our results showed that the model predicted values agreed with the theoretical values within 1% difference. The DMC model results are comparable with experimental results within 5% differences.

Keywords: Photo-cured dental composite, depth of cure, dynamic optical property, photon propagation

1. INTRODUCTION

Photo-cured polymers have been used in a wide variety of areas, such as on UV photocurable coatings industry,[1] orthopedic biomaterials,[2] and dental restorations.[3] The particular advantage of a photo-cured polymer used as a biomaterial is its potential for *in situ* formation, which allows for the filling of irregular shaped target defects (for example, cavities in the teeth), allows for spatial and temporal control of the polymerization, and allows rapid polymerization under physiological conditions. A critical feature of a photo-cured polymer is the extent of cure, which affects the mechanical or physical properties of the composite restorative, such as the hardness, the fracture toughness, or the shrinkage.

Photoinitiators are designed to absorb light and produce radicals. This absorption causes significant light attenuation (especially when polymerizing thick samples), which decreases the rate of polymerization, and causes insufficient extent of cure at deeper depths. Previous studies[4] showed that during the curing process, absorption by the photoinitiator declines as the initiator is incorporated into the polymer through an addition process. The refractive index of the resin matrix also changes during the polymerization,[5] which in turn affects the scattering by the filler particles, thereby changing the overall scattering coefficient of the composite. Thus, the distribution of light within the composite changes as it cures.

The distribution of light in a multiply scattering medium depends on the scattering and absorption coefficients as well as on the index of refraction. Previous research has shown that a simple Monte Carlo model can be used to simulate light transport in static optical property media to understand the light distribution in the dental

Further author information: (Send correspondence to S. A. P.)
Y.-C. C.: E-mail: yinchu@bme.ogi.edu, Tel: (503) 216-6830
S. A. P.: E-mail: prahl@bme.ogi.edu, Tel: (503) 216-2197

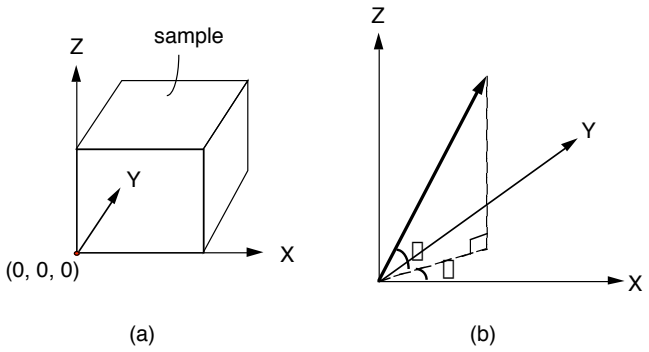

Figure 1. The trajectory of the photon in Cartesian coordinates.

composites.[4] However, in reality, the optical properties of photocured dental composites change during the curing process. A more complicated dynamic Monte Carlo model that allows for the changes in optical properties as the photon is absorbed is needed to describe accurately the light distribution in the composite as it cures.

Several attempts have been made to develop Monte Carlo models that account for local changes in absorption and scattering coefficients due to laser irradiation but these models were either two-dimensional[6] or assumed a spherical geometry.[7] A three-dimensional modular adaptive grid numerical model by Pfefer *et al.* was developed to simulate the light propagation in geometrically complex biological tissues.[8] Their model allowed the optical properties to be varied within structurally complex biological tissue by digitally mapping the structure of different biological tissues with the fine symmetrical grids they created, but their model was not adapted for dynamic changes of optical properties during the photon deposition.

This study developed a dynamic Monte Carlo (DMC) model for heterogeneous media whose optical properties can vary with position and can vary dynamically as photons are absorbed. The DMC model was verified numerically with theoretical and experimental results.

2. DYNAMIC MONTE CARLO MODEL (DMC) METHODS

2.1. Initialization

This Monte Carlo program uses Cartesian coordinates (x, y, z) to represent the location of the photons. The dimensions of the medium and the bin size are specified explicitly. Each bin is the same size. Each of the Cartesian locations is converted to the bin index based on the bin size. Each bin is assigned an initial set of optical properties. The trajectory of the photon is represented by the direction cosines as (u_x, u_y, u_z),

$$u_x = \cos(\theta)\cos(\varphi) \ ,$$

$$u_y = \cos(\theta)\sin(\varphi) \ ,$$

$$u_z = \sin(\theta) \ ,$$

where θ is the polar angle from the z-axis and φ is the azimuthal angle in the xy-plane from the x-axis in spherical coordinate (Fig. 1). Each direction cosine is the cosine of the angle between the current photon direction and the respective axis.

2.2. Photon movement

A circular flat beam was launched perpendicular to the top surface. Each launched photon begins with a full weight, one minus the specular reflection, at the surface (see section 2.3). As the photon moves, its weight attenuates with its path length based on the Beer's law. The step size S is chosen as the distance to the next scattering event,

$$S = -\ln(\xi)/\mu_s \ ,$$

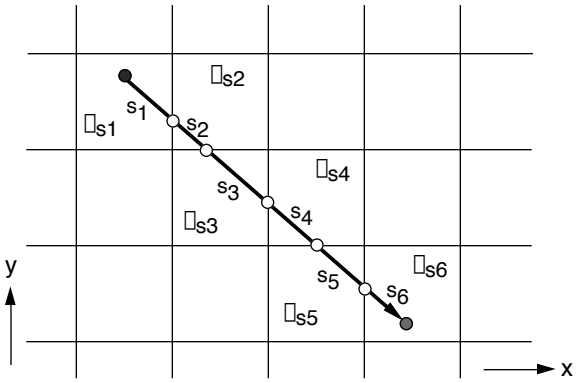

Figure 2. A 2-D representation of photon taking steps. The photon take one step to cross one bin at a time (s_1, s_2, ..., or s_6) until $-\ln(\xi) = s_1\mu_{s1} + s_2\mu_{s2} + s_3\mu_{s3} + \ldots + s_6\mu_{s6}$, where ξ is a random number between 0 and 1, and $\mu_{s1,2,\ldots,6}$ are the scattering coefficients of the bins.

where ξ is a non-zero random number between 0 and 1, and μ_s is the scattering coefficient of the bin which currently contains the photon. However, since the optical properties may vary from bin to bin, instead of moving the photon a distance S to the next scattering event, the photon moves one bin at a time until the accumulated step size matches $S \cdot \mu_s$ (see Fig. 2 for a 2-D representation). In other words,

$$-\ln(\xi) = s_1\mu_{s1} + s_2\mu_{s2} + s_3\mu_{s3} + \ldots + s_n\mu_{sn} \quad ,$$

where $s_1, s_2, \ldots, s_n$ are the step sizes within each bin, and $\mu_{s1}, \mu_{s2}, \ldots, \mu_{sn}$ are the scattering coefficients of these bins. Note that the photon may not be able to take a full step from one bin to another at the last step s_n. Therefore, s_n is the residual step left after the $n-1$ steps.

The calculation of the step size $s_1, ..., s_n$ is the most significant addition of this Monte Carlo program. To begin, the closest of the six planes along the photon trajectory must be found. An example of a photon movement is presented in Fig. 3. According to the signs of (u_x, u_y, u_z), we know the direction in which the photon will go. For example, in Fig. 3, the photon is directed forward ($u_y > 0$) to the right ($u_x > 0$) and upwards ($u_z > 0$). To discover which plane of the bin that the photon hits first (e.g., plane 1, 2, or 5 in this example), we use the trajectory in the $\vec{x}$-$\vec{y}$ plane to calculate the distance (Δv) to the edge of the bin in the $\vec{x}$-$\vec{y}$ plane and then judge which plane is hit in the trajectory $\vec{v}$-$\vec{z}$ plane. The distances to each of the remaining planes ($\Delta x_1, \Delta x_2, \Delta y_1, \Delta y_2, \Delta z_1$, and Δz_2) are used to calculate the angles, δ in $\vec{x}$-$\vec{y}$ plane (Fig. 3(b)) and α in trajectory $\vec{v}$-$\vec{z}$ plane (Fig. 3(c)). In this example,

$$\delta_1 = \tan^{-1}(\Delta y_1/\Delta x_1).$$

The azimuthal angles, φ and δ_1 (Fig. 3(b)), are first compared to decide the movement to plane 1 or plane 2 and to calculate the moving distance Δv in $\vec{x}$-$\vec{y}$ plane. If $\varphi \leq \delta_1$, move to plane 1 and $\Delta v = \Delta x_1/\cos\varphi$; otherwise, move to plane 2 and and $\Delta v = \Delta y_1/\sin\varphi$.

Subsequently, the polar angles, θ and α_1 (Fig. 3(c)), in the trajectory $\vec{v}$-$\vec{z}$ plane is compared to decide the movement to plane 2 or plane 5 and to calculate the step size, s_1, for the photon. In this example,

$$\alpha_1 = \tan^{-1}(\Delta z_1/\Delta v).$$

If $\theta \leq \alpha_1$, move to plane 2 and $s_1 = \Delta v/\cos\theta$; otherwise, move to plane 5 and and $s_1 = \Delta z_1/\sin\theta$.

After the step size of the photon is found, the photon position is updated from the old position (x, y, z) to a new position (x', y', z') as following equations,

$$x' = x + s_1 u_x \quad ;$$
$$y' = y + s_1 u_y \quad ;$$
$$z' = z + s_1 u_z \quad .$$

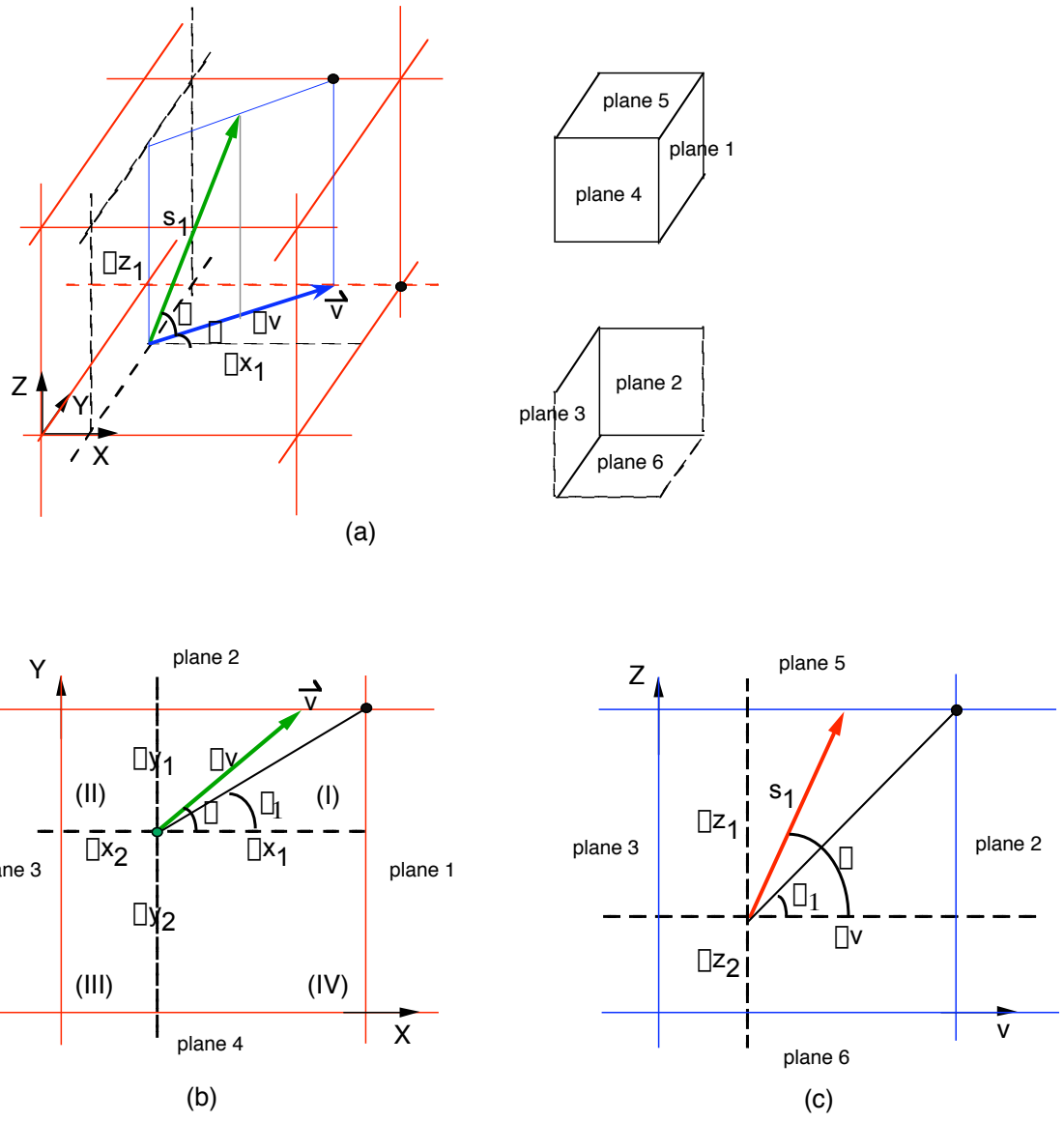

Figure 3. A schematic drawing of photon movement to the boundary plane of a bin. The azimuthal angle of the trajectory is φ, and the polar angle is θ. The distances is Δx_1 to plane 1, Δx_2 to plane 3, Δy_1 to plane 2, Δy_2 to plane 4, Δz_1 to plane 5, and Δz_2 to plane 6. Figure (a) is a 3-D representation of photon movement. The projector of the trajectory in the $\vec{x}$-$\vec{y}$ plane is $\vec{v}$, and the distance to the edge of the bin is Δv. Figure (b) is a 2-D representation of the trajectory projected in the $\vec{x}$-$\vec{y}$ plane. $\delta_1 = \tan^{-1}(\Delta y_1/\Delta x_1)$. $\Delta v = \Delta y_1/\sin\varphi$. Figure (c) is a 2-D representation of the trajectory in the trajectory $\vec{v}$-$\vec{z}$ plane. $\alpha_1 = \tan^{-1}(\Delta z_1/\Delta v)$. $s_1 = \Delta z_1/\sin\theta$.

2.3. Drops of weight

By moving a distance of s_1, the weight of the photon (W_{new}) becomes

$$W_{new} = W_{old} \exp(-\mu_{a1} s_1) \ ,$$

where μ_{a1} is the absorption coefficient of the bin that the photon crosses. The reduced weight is deposited to the local bin that the photon just travels through.

2.4. Boundary conditions

When the photon travels to the outer boundary of the medium, the photon will be terminated and drop any remaining weight in the edge bin the photon was in. When the photon travels to the top or bottom surface of the medium, there are two possible results. If the incident angle θ_i is greater than the critical angle θ_c, the photon will be totally reflected; otherwise, the photon is partially reflected back to the medium where the Fresnel equation (Eq. 1) will be applied.

$$\theta_c = \sqrt{1 - \frac{1}{n^2}} \ ,$$

where n is the refractive index of the medium. The Fresnel reflectance R is

$$R = \frac{1}{2}(R_{\parallel} + R_{\perp}) \ , \tag{1}$$

where

$$R_{\parallel} = \frac{\tan^2(\theta_i - \theta_t)}{\tan^2(\theta_i + \theta_t)} \quad \text{and} \quad R_{\perp} = \frac{\sin^2(\theta_i - \theta_t)}{\sin^2(\theta_i + \theta_t)} \ ,$$

where θ_i is the incident angle and θ_t is the transmission angle.

2.5. Changes of optical properties

After the weight of the local bin has been updated, the optical properties of the local bin are updated based upon how much light is absorbed, that is the relationship between the optical properties and radiant exposure. The radiant exposure H in each bin is calculated as

$$H = \frac{W_{\text{total}}}{N v \mu_a} \cdot EA \ ,$$

where W_{total} is the totally deposited weight, N is number of photons/sec, v is the bin volume, μ_a is the absorption coefficient at that bin, E is irradiance of the illumination, and A is the area of the illumination beam.

2.6. Check photon status

The weight of the photon attenuates as the photon moves; however, the weight never goes to zero. Therefore, we set a weight minimum threshold to terminate the photons if the weight of the photon drops below this threshold.

3. DMC MODEL VERIFICATION

Verification of the DMC model was done by comparing the DMC results with numerical results for absorption only media, and with the measurements on the optical property changes of unfilled resins.[9]

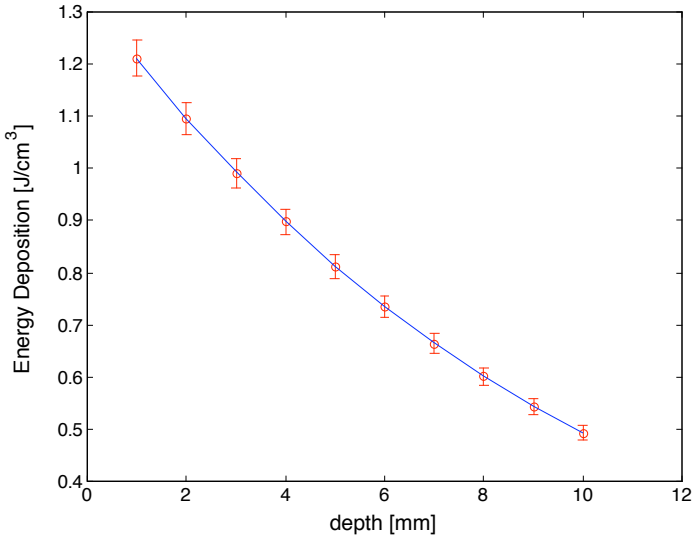

Figure 4. Comparison of theoretical deposited energy density Eq. 3 (line) and simulation results (circle) for 1 J, 1 cm diameter light beam into $\mu_a = 1\,\mathrm{cm}^{-1}$ medium with matched boundaries. Each of the error bars is the standard deviation of 5 simulations, each of which is 200,000 photons.

3.1. Absorption only media

Three types of absorption properties were simulated:

1. Simple, fixed absorption coefficient media:
   (a) For 1 J beam going through $\mu_a = 2\,cm^{-1}$, refractive index n_m=1.5, ℓ=1 cm thick media, the specular reflectance of the beam is
   $$\mathrm{sr} = \left(\frac{n_m - n_{air}}{n_m + n_{air}}\right)^2 \quad . \tag{2}$$
   So, the theoretical total reflectance R and transmission T should be
   $$R = \frac{\mathrm{sr}}{1-(1-\mathrm{sr})^2 e^{-2\mu_a \ell}} = 0.04069 \quad \text{and} \quad T = \frac{(1-\mathrm{sr})^2 e^{-\mu_a \ell}}{1-\mathrm{sr}^2 e^{-2\mu_a \ell}} = 0.12473 \quad .$$
   The DMC model generates $R = 0.04068(6)$, and $T = 0.12473(2)$ for five simulations of 200,000 photons.
   (b) For a 1 J, r=0.5 cm radius light beam launched into $\mu_a = 1\,\mathrm{cm}^{-1}$, n_m=1 medium, the theoretical deposited energy density at the ith layer with thickness Δx =0.1 cm is
   $$W_i = \left(e^{-\mu_a (i-1)\Delta x} - e^{-\mu_a i \Delta x}\right)/V \quad , \tag{3}$$
   where i is the layer number 1,2,...,10, and V=$\pi r^2 \Delta x$ is the volume of the deposited unit . It shows that the DMC results match this numerical result (shown in Fig. 4).

2. Layered absorption coefficient media:
   A 1 J, r=0.5 cm radius light beam was launched into a n_m=1.5 medium whose absorption increases with depth: $\mu_{a,i} = ik\,\mathrm{cm}^{-1}$, where the increasing rate k is 0.2 and i is the layer number 1,2,...,10. Each layer is Δz=0.1 cm thick. The theoretical energy density at ith layer is
   $$W_i = \frac{1-\mathrm{sr}}{V}\left(\exp[\frac{-i(i-1)k}{2}] - \exp[\frac{-i(i+1)k}{2}]\right) \quad , \tag{4}$$

where sr can be calculated from Eq. 2 and $V = (\pi r^2 \Delta z)\,\mathrm{cm}^3$. The comparison in Fig. 5 shows that the DMC results match the numerical results.

3. Dynamic absorption coefficient media:
Assume $1\,\mathrm{W/cm^2}$ light beam was illuminated into a medium whose absorption coefficient dynamically changes with deposited energy density:

$$\mu_{a,j}(t) = 1 - kW_j(t) \quad \mathrm{cm}^{-1} \ , \tag{5}$$

where k=0.05 and $W_j(t)$ is jth-layer deposited energy density as a function of time t. Assume the layer thickness is Δz, then the irradiance at bottom of jth layer is

$$I_j = I_0 \prod_{i=1}^{j} \exp(-\mu_{a,i}\Delta z) \ .$$

Therefore,

$$W_j(t) = W_j(t - \Delta t) + \frac{\Delta t}{\Delta z} I_0 (1 - \exp(-\mu_{a,j}\Delta z)) \prod_{i=1}^{j-1} \exp(-\mu_{a,i}\Delta z) \ .$$

The final deposited energy density W_{DMC} in each bin was calculated as

$$W_{\mathrm{DMC}} = w/Nv \quad [\mathrm{J/cm}^3],$$

where w is the total weight in each bin, $N = 4 \cdot 10^4\,\mathrm{photons/J}$, and v is the bin volume. In all the simulations, the energy density and the absorption coefficient at each time point and each layer were recorded for comparison. Figure 6 compares the results of $W(t)$ and $\mu_a(t)$ at four different depths. Figure 7 compares the results of W_j and $\mu_{a,j}$ at five time points. The DMC results match the numerical model within 1% difference.

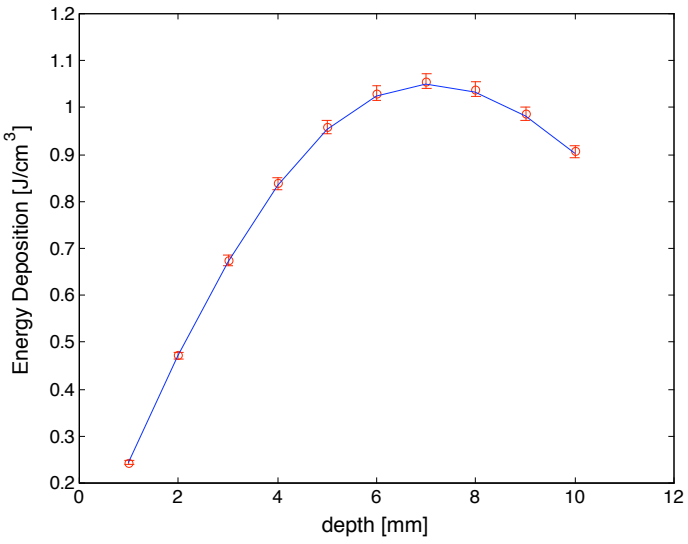

Figure 5. Comparison of theoretical deposited energy density Eq. 4 (line) and simulation results (circle) for 1 J, 1 cm diameter light beam into $\mu_{a,i} = 0.2i\,\mathrm{cm}^{-1}$ medium with specular reflection, where i is the layer number, 1, 2, ..., 10. Each layer is 0.1 cm thick. Each of the error bars is the standard deviation of 5 simulations, each of which is 200,000 photons.

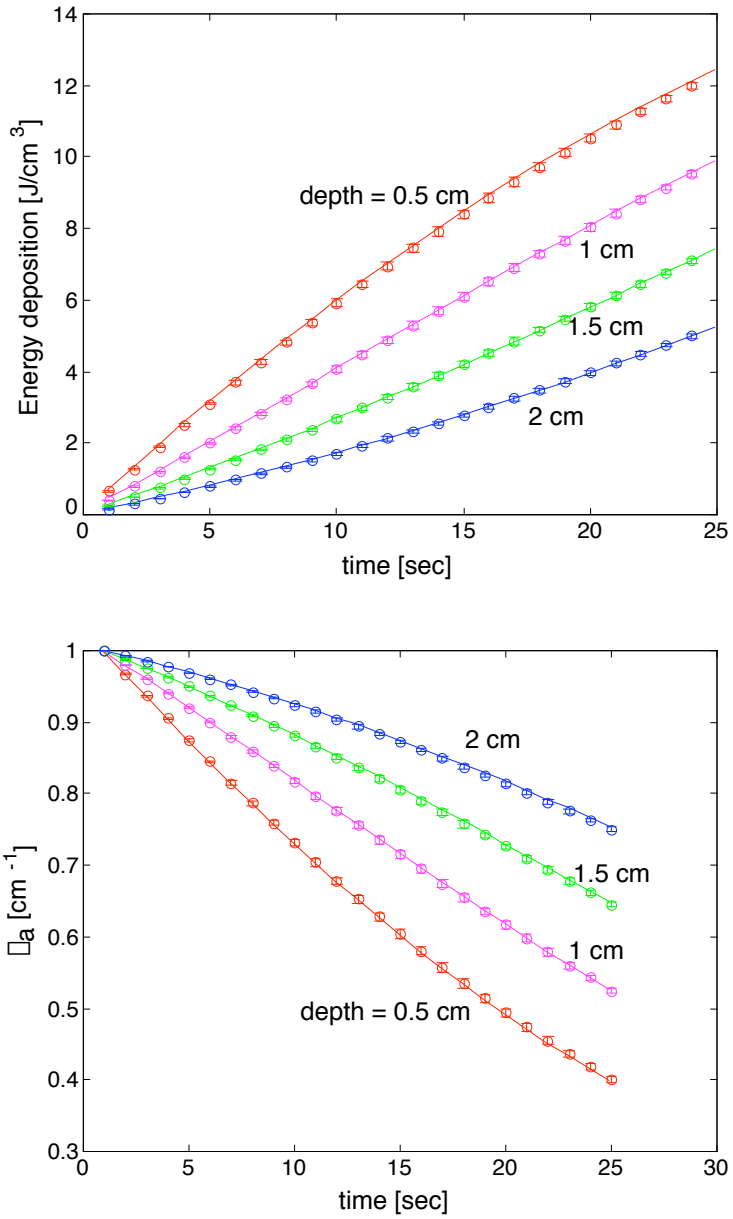

Figure 6. Comparison of numerical (line) and simulation results (circle) for 1 J/cm^2 light beam into dynamic absorption coefficient medium (Eq. 5). The top figure depicts the deposited energy density versus time at 4 different depths. The bottom figure depicts the absorption coefficients versus time at 4 depths. Each errorbar is the standard deviation of 4 simulations, each of which is 1 million photons.

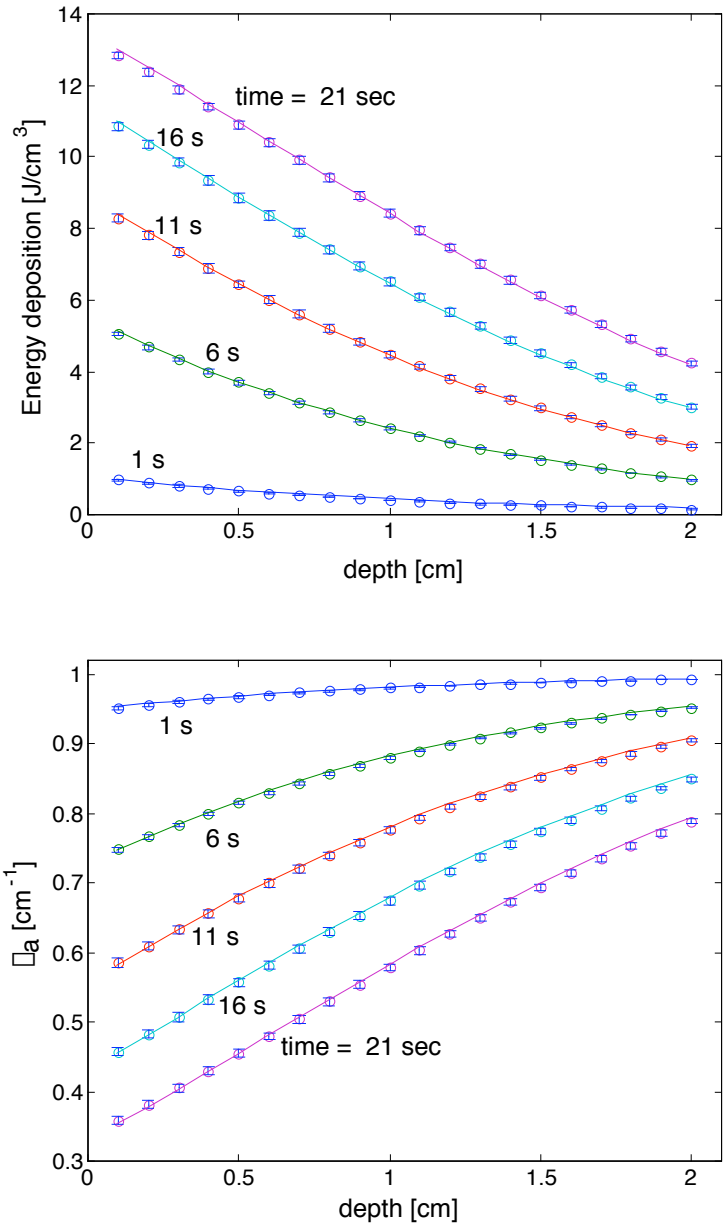

Figure 7. Comparison of numerical (line) and simulation results (circle) for 1 W/cm^2 light beam into dynamic absorption coefficient medium (Eq. 5). The top figure depicts the deposited energy density versus depth at 5 different times. The bottom figure depicts the absorption coefficients versus depth at 5 times. Each errorbar is the standard deviation of 4 simulations, each of which is 1 million photons.

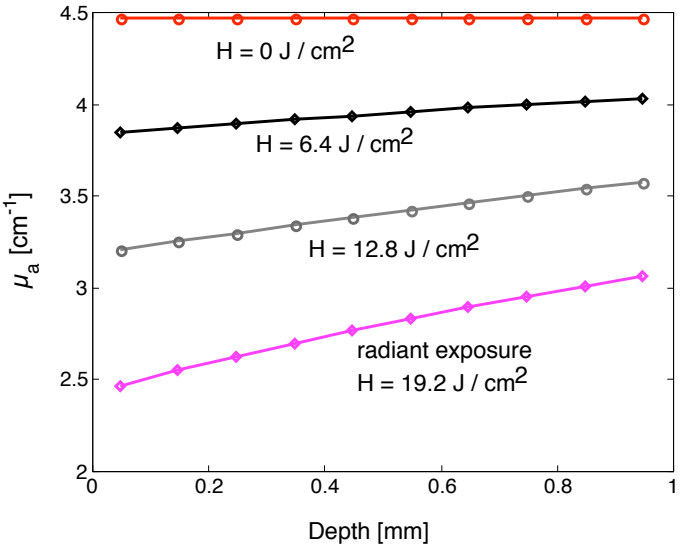

Figure 8. DMC model results of resin μ_a as a function of depth at different radiant exposures.

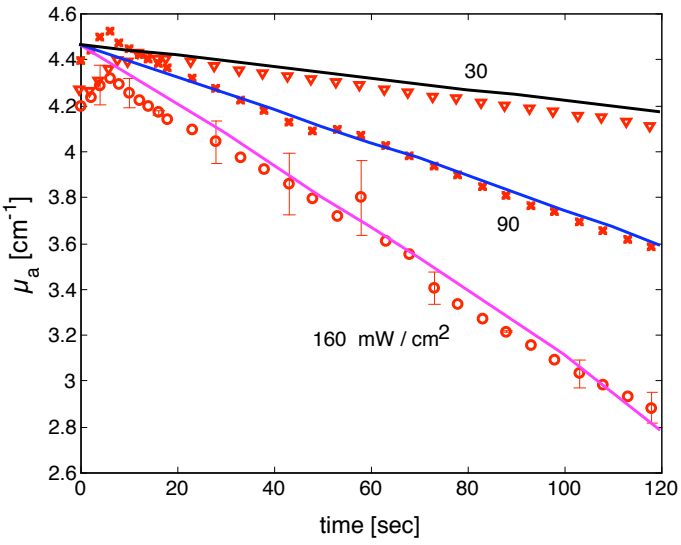

Figure 9. Comparison of DMC model results (lines) and the experimental results (points) from Chapter 6 for resin μ_a as a function of irradiation time for three different irradiances: 160, 90, and 30 $\mathrm{mW/cm^2}$.

3.2. Simulation of unfilled resin during curing

Based on the μ_a and radiant exposure H relationship[9]:

$$\mu_a(H) = \mu_{ao} \exp(-H/H_{\text{total}}) \quad , \tag{6}$$

we simulated the μ_a of resin as a function of radiant exposure and compared the results with the experimental measurements.[9] Three simulations were performed for the three irradiances: 160, 90, and 30 mW/cm^2. The μ_{ao} was 4.46 cm^{-1} and H_{total} was 43 J/cm^2, and a thickness of 1 mm resin was assumed. The light illumination was assumed to be collimated, flat, and circular. The μ_a at different depths, the total reflectance and transmission were recorded every 10 seconds for total of 120 seconds. Note that all the simulation parameters were assumed at 469 nm wavelength.

The change of resin μ_a as a function of depth at different radiant exposure with increments of 6.4 J/cm^2 is shown in Fig. 8. Note that the radiant exposure H here is the H at the top surface, not the actual H at each depth. The μ_a of the top layer is about 30% lower than the bottom μ_a after 19 J/cm^2 of exposure. Assume that the average of the μ_a throughout the depth represents the μ_a of the whole resin. The μ_a as a function of curing time for the three irradiances is plotted in Fig. 9 and compared with the experimental results from our previous studies.[9] The overall differences between the model and experimental results were less than 5%.

4. DISCUSSION

Verification of the DMC model has been made by comparing with the analytical solutions and the experimental results from our previous studies.[9] The reflectance and transmittance results produced by the DMC for the simplified absorption only cases were within 0.05% of differences to the analytical solutions. The simulation results of dynamic absorption property media were within 1% of the numerical models (Fig. 6 and 7). The simulation results of the dynamic absorption coefficient of unfilled resin during curing showed good agreement with the experimental results with only 5% differences (Fig. 9). The errors are the combination of experimental errors and statistic deviations in the model.

While the DMC model was able to simulate heterogeneous media with dynamic optical properties, the computational effectiveness may be a consideration for using this model. The dimension of the media, the bin sizes, the number of photons per recording time, and the absorption and scattering coefficient values all affect the simulation time. Increasing the resolution on the grid sizes will increase the accuracy of the local energy deposition and optical property changes, but will increase statistical variations since fewer photons are deposited per bin. One advantage of this DMC code is that the dimension of the bins can be nonsymmetrical. Therefore, for $x-y$ symmetrical system, one can have finer grid sizes along the light illumination depth (e. g. z direction) and larger grid sizes in the $x-y$ dimension. In this way, the calculation rate can be increased. To get the simulation results shown in Fig. 9 using the DMC code, the propagation of a total of 100,000 photons required approximately 1 minutes of processor time on a Mac G3 500 MHz processor computer.

In conclusion, this study has shown that the DMC model can be used to simulate the light transport in a photocured material that has dynamical optical properties. The time-resolved energy deposition and optical property distributions in the materials, as well as the time-resolved reflectance and transmittance can be calculated during photon absorption.

ACKNOWLEDGMENTS

This work was supported by the grants from National Institute of Health, Grant NIH-CI-R24-CA84587-04 and NIH-NIDCR-DE07079.

REFERENCES

1. J. V. Koleske, "A radiation-cure primer," *J. Coat. Technol.* **69**, pp. 29–38, 1997.
2. J. A. Burdick, A. J. Peterson, and K. S. Anseth, "Conversion and temperature profiles during the photoinitiated polymerization of thick orthopaedic biomaterials," *Biomaterials* **22**, pp. 1779–1786, 2001.

3. E. P. Allen, S. C. Bayne, A. H. Brodine, R. J. Cronin Jr, T. E. Donovan, J. C. Kois, and J. B. Summitt, "Annual review of selected dental literature: report of the committee on scientific investigation of the American academy of restorative dentistry," *J. Prosthet. Dent.* **90**, pp. 50–80, 2003.
4. Y. C. Chen, F. L. Ferracane, and S. A. Prahl, "A photon migration model for predicting depth of cure in dental composite," *Dent. Mater.* , submitted.
5. O. Dudi and W. T. Grubbs, "Laser interferometric technique for measuring polymer cure kinetics," *J. Appl. Polym. Sci.* **74**, pp. 2133–2142, 1999.
6. S. Rastegar, B. Kim, and S. L. Jacques, "Role of temperature dependence of optical properties in laser irradiation of biological tissue," vol. 1646, pp. 228–231, SPIE, 1992.
7. L. C. Chin, W. M. Whelan, and I. A. Vitkin, "Models and measurements of light intensity changes during laser interstitial thermal therapy: implications for optical monitoring of the coagulation boundary location," *Phys. Med. Biol.* **48**, pp. 543–559, 2003.
8. T. J. Pfefer, J. K. Barton, E. K. Chan, M. G. Ducros, B. S. Sorg, T. E. Milner, J. S. Nelson, and A. J. Welch, "A three-dimensional modular adaptable grid numerical model for light propagation during laser irradiation of skin tissue," *IEEE J. Sel. Top. Quant.* **2**, pp. 934–942, 1996.
9. Y.-C. Chen, F. L. Ferracane, and S. A. Prahl, "Quantum yield of conversion of the dental photoinitiator camphorquinone," SPIE saratov Fall meeting, 2004.